A Spin Frustrated Hourglass {Gd_9} Molecular Nanomagnet with unusual magnetocaloric properties

Sai P. K. Panguluri[a], Eufemio Moreno-Pineda[*,b,c,d], Concepción Molina-Jirón[a,d,e], Sagar Paul[b], Marc Ubach I. Cervera[f], Emmanouil K. Charkiolakis[f], David Gracia[f], Marco Affronte[g,h], Wolfgang Wernsdorfer[a,b], Marco Evangelisti[*,f], Jürgen Schnack[*,i] and Mario Ruben[*a,j,k]

a. *Institute of Quantum Materials and Technologies (IQMT), Karlsruhe Institute of Technology (KIT), Hermann-von-Helmholtz-Platz 1, 76344, Eggenstein-Leopoldshafen, Germany.*
b. *Physikalisches Institut, Karlsruhe Institute of Technology, D-76131, Karlsruhe, Germany.*
c. *Universidad de Panamá, Facultad de Ciencias Naturales, Exactas y Tecnología, Depto. de Química-Física, 0824, Panamá.*
d. *Universidad de Panamá, Facultad de Ciencias Naturales, Exactas y Tecnología, Grupo de Investigación de Materiales, Panamá, 0824, Panamá*
e. *Universidad de Panamá, Facultad de Ciencias Naturales, Exactas y Tecnología, Depto. de Bioquímica, 0824, Panamá.*
f. *Instituto de Nanociencia y Materiales de Aragón (INMA), CSIC & Universidad de Zaragoza, C/ Pedro Cerbuna 12, 50009 Zaragoza (Spain).*
g. *Dipartimento di Scienze Fisiche, Informatiche e Matematiche, Universita di Modena e Reggio Emilia, via G. Campi 213/a, Modena, 41125, Italy.*
h. *Istituto Nanoscienze, CNR, via G. Campi 213/a, Modena, 41125, Italy.*
i. *Bielefeld University, Faculty of Physics, D-33615 Bielefeld, Germany*
j. *Institute of Nanotechnology (INT), Karlsruhe Institute of Technology (KIT), Kaiserstraße 12, D-76131 Karlsruhe, Germany*
k. *Instituto de Ciencia de Materiales de Aragón and Departamento de Física de la Materia Condensada, CSIC-Universidad de Zaragoza, 50009 Zaragoza (Spain).*
l. *Centre Européen de Sciences Quantiques (CESQ), Institut de Science et d'Ingénierie Supramoléculaires (ISIS), 8 allée Gaspard Monge, BP 70028, 67083, Strasbourg Cedex, France.*

*Correspondence to: eufemio.moreno@up.ac.pa; evange@unizar.es; jschnack@uni-bielefeld.de; mario.ruben@kit.edu

KEYWORDS: magnetocaloric, isentropes, heat capacity, spin frustration, competing interactions, Lanczos method.

ABSTRACT: *We report a highly symmetric **{Gd_9}** molecular nanocage with the formula $[Gd_9(BA)_{16}(OH)_{10}]Cl\cdot 3(C_2H_5OH)\cdot 4(H_2O)$, which crystallizes in the cubic space group $Pn\bar{3}n$. The structure features two crystallographically distinct Gd^{3+} ions, forming highly regular triangular Gd^{3+} arrangements leading to a geometrically frustrated magnetic network. Magnetisation measurements at 2 K reveal a broad plateau between 1.5 and 4 T, while zero-field heat capacity shows a Schottky anomaly centred at 0.6 K—indicative of low-lying excited states and competing magnetic interactions. The magnetocaloric effect, evaluated through both direct and indirect methods, exhibits a re-entrant profile in the isentropic curves, pointing to a non-trivial evolution of magnetic entropy under applied fields. To probe the origin of this behavior, we employed the finite-temperature Lanczos method on a model spin Hamiltonian. The results reveal that the antiferromagnetic exchange between Gd^{3+} ions, combined with the frustration inherent to the **{Gd_9}** geometry, leads to a degenerate ground state. An external field lifts this degeneracy, producing a regime with a sharply reduced density of states between 1.5 and 4 K, which underlies the unconventional magnetocaloric response. The **{Gd_9}** cage thus represents a rare example spin-frustrated arrangement arising from competing antiferromagnetic interactions between the Gd^{3+}. These findings demonstrate how frustrated topologies and tunable low-energy excitations can be exploited to modulate the magnetothermal properties, with potential implications for cryogenic magnetic cooling technologies.*

INTRODUCTION

In magnetic systems, the impossibility of simultaneously satisfying pairwise interactions gives rise to frustration, typically due to geometric or exchange constraints[1,2]. Geometric spin frustration—where the topology of the lattice alone prevents the full minimization of exchange energies—suppresses classical magnetic order and stabilizes a range of unconventional ground states[1]. This phenomenon is especially pronounced in triangular lattices[3–5], where antiferromagnetic coupling among half-integer spins in odd-membered rings creates a macroscopically degenerate manifold.

Crucially, such behavior is not confined to extended lattices: zero-dimensional molecular architectures, particularly coordination compounds, frequently incorporate triangular spin motifs[6–9]. These discrete systems offer synthetically tunable platforms for probing frustration at the molecular scale[10]. Frustrated molecular nanomagnets (FMN) are increasingly recognized as promising candidates for magnetocaloric applications. Their discrete energy spectra, well-defined spin states, and chemical modularity allow fine control over magnetic entropy[11–13]. Moreover, spin frustration enhances the magnetocaloric effect (MCE) at low temperatures by broadening the temperature range of paramagnetic-like behavior. Besides, it increases the density of low-lying spin states and enables field-tunable degeneracies, resulting in large isothermal entropy changes and pronounced adiabatic temperature shifts under applied magnetic fields—key performance metrics in solid-state refrigeration[6].

The investigation of molecular nanomagnets for sub-kelvin magneto refrigeration typically relies on isotropic ions with large magnetic moments[8,12–17], although anisotropic systems[18,19] can likewise be considered. However, unlike paramagnetic salts, FMN exhibits complex magnetothermal behavior arising from internal exchange interactions and quantum level crossings[2]. These phenomena, associated with quantum phase transitions, enable sharp entropy redistributions that amplify the MCE. Additionally, frustration preserves residual entropy at zero temperature, enabling rapid cooling near the saturation field[20–22]. On the quest for further understanding of frustration effects on FMN, here, we investigate a highly symmetric molecular cage, with formula $[Gd_9(BA)_{16}(OH)_{10}]Cl{\cdot}3(C_2H_5OH){\cdot}4(H_2O)$ (where BA = Benzoylacetonate (**{Gd_9}**) with an hourglass-like molecular structure (**Figure 1**). The complex, featuring four **{Gd_3}** vertex-sharing triangular Gd^{3+} motifs, displays frustration of its energy manifold; hence, it exhibits a strongly field-dependent density of states and a tunable magnetocaloric response, highlighting the importance of the energy landscape engineering for molecular coolants.

RESULTS AND DISCUSSION

The hourglass-like complex crystallizes in the $Pn\bar{3}n$ space group, with six cationic **{Gd_9}** cages residing per unit cell. Three differently oriented molecules compose the unit cell, with the shortest Gd···Gd distance being 12.904 Å (See **Figure S1**). The asymmetric unit represents one-eighth of the molecule, indicating that the complete cage exhibits S_8 symmetry. The **{Gd_9}** cage consists of two pentanuclear square pyramids sharing a central Gd^{3+} ion, forming an hourglass-like shape (**Figure 1C,D**). These pyramids are twisted relative to each other by about 45°, resulting in a square antiprismatic geometry at the central Gd^{3+} ion (**Figure 1B**).

Single-crystal X-ray diffraction reveals that the cage contains only two distinct types of Gd^{3+} ions: the central ion (Gd(1)) is octacoordinated, possessing a nearly perfect square antiprismatic geometry with D_{4d} symmetry, as confirmed by Continuous

Shape Measures[23] (CShM, **Table S1**). Its coordination sphere consists exclusively of eight μ_3-OH^- groups; the eight peripheral ions (Gd(2)), also octacoordinated, but with a more irregular geometry. Each Gd^{3+} ion is chelated by three BA^- ligands—two with coordination mode μ-BA(κ²O,O';κ¹O) and one with μ-BA(κ²O,O')—along with two μ_3-OH^- groups. These ions adopt a trigonal dodecahedral geometry with D_{2d} symmetry (**Table S1**).

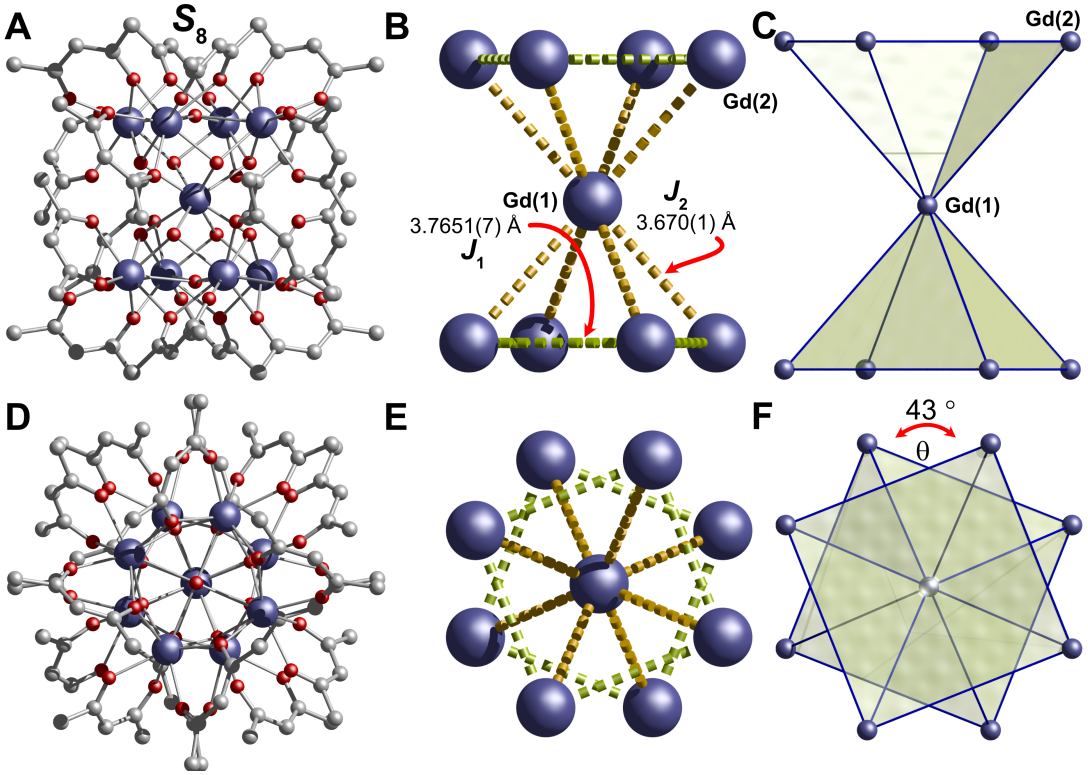

Figure 1. Crystal structure of $[Gd_9(BA)_{16}OH_{10}]Cl$ **{Gd_9}** side (**A**,**B**,**C**) and top view (**D**,**E**,**F**), highlighting the highly regular structure with triangular Gd^{3+} arrangements. The yellow and green dotted lines in panels **B** and **E** depict the two different interactions occurring in the **{Gd_9}** cage. Color code: Gd, blue; O, red; C, grey. Hydrogens omitted for clarity.

The metallic core of the **{Gd_9}** cage can also be described as a pyramidal assembly of four **{Gd_3}** triangles, each formed by one Gd(1) and two Gd(2) ions. These triangles share Gd(1) as a common vertex, while also sharing edges with adjacent triangles. Each Gd(2) is stabilized by a μ_3-OH^- bridge and is collectively capped by a μ_4-OH^- group at the base of the pyramid. The Bond Valence Sum (BVS) for the μ_3-OH^- is found to be 1.073, while for the μ_4-OH^-, the BVS is 1.02, both being consistent with OH^- groups[24]. The overall complex is charge-balanced by a Cl^- ion. Due to the highly symmetric triangular arrangement of Gd^{3+} ions within the **{Gd_9}** cage, magnetic frustration effects are likely to occur.

To explore how the highly regular **{Gd_9}** cage influences the magnetic behavior, we conducted magnetic susceptibility ($\chi_M \equiv M/B$) measurements. The χ_M properties were collected employing a polycrystalline sample under an applied field of 0.1 T in the temperature range of 2-300 K (top panel in **Figure 2**). At room temperature, the $\chi_M T$ value amounts to 67.4 emu K mol^{-1}, in line with nine $^8S_{7/2}$ ions (cf. 68 emu K mol^{-1} for nine non-interacting s = 7/2 ions with g = 1.96). As the temperature decreases, the $\chi_M T(T)$ remains nearly constant down to ca. 20 K, where it sharply drops to 29.3 emu K mol^{-1}. The downturn is indicative of antiferromagnetic interactions within the cage, as commonly observed in systems with similarly highly symmetric motifs.

Magnetization studies (M) were conducted in the temperature range of 2–10 K and with applied fields between 0 and 7 T. The $M(B,T)$ data shows that saturation is achieved for

fields above 6 T (bottom panel in **Figure 2**). Remarkably, a plateau is also observed between 1.5 and 4 T for the $M(B)$ traces below 3 K. Note that such a type of plateau is uncommon in lanthanide-based complexes and is a signature of spin frustration effects[2]. To further investigate the system, we employed μSQUID arrays from 5 K down to 30 mK, in the field range of ±1.4 T. No major structure is revealed in the $M(B)$ loops. Notably, the $M(B)$ loops above 2 K, however, yield a vanishing magnetic signal, likely due to the large density of populated states at such temperature and field, a signature of frustration (See **Figure S3**).

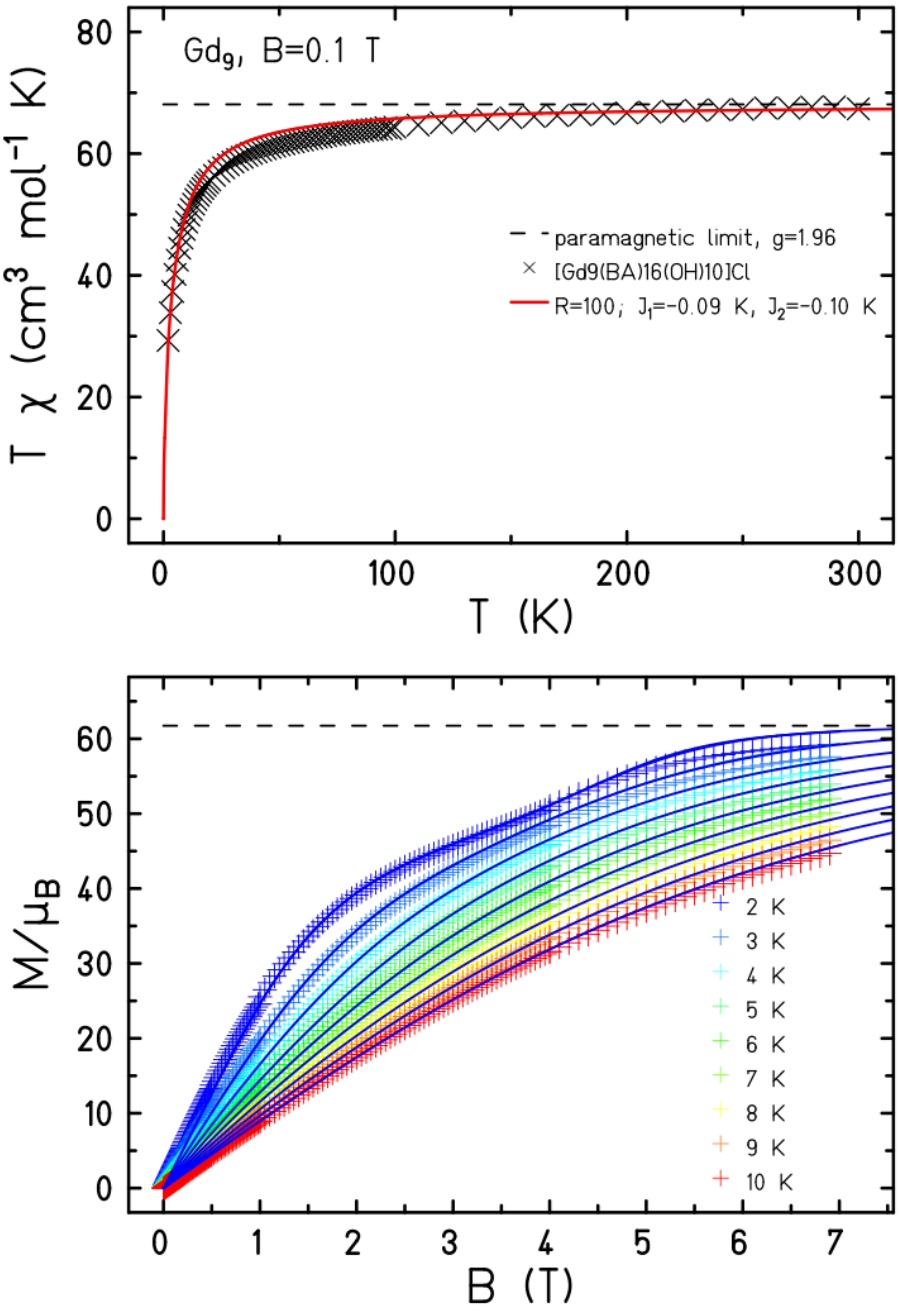

Figure 2. Magnetic susceptibility versus temperature ($\chi_M T$, T) at B = 0.1 T (top) and magnetization versus applied magnetic field (M, B) for temperatures from 10 down to 2 K (bottom). R is the number of random vectors employed for the computation. The experimental data are given by symbols, while the theoretical calculations are shown by curves (see text).

A better insight into the magnetic characteristics of **{Gd$_9$}** can be gained by conducting field-dependent heat capacity (c_p) studies. These studies are a powerful

tool for probing spin frustration in molecular nanomagnets, since they sensitively capture low-energy excitations and quantum level crossings, offering insight into the system's magnetic energy landscape[5–7,17]. The c_p response of **{Gd$_9$}** under different magnetic fields was investigated between 30 K and 50 mK with fields up to 7 T (**Figure 3**).

In the temperature range above liquid helium, c_p is predominantly influenced by the nonmagnetic lattice contribution, which can be effectively represented by the Debye function. This analysis leads to the determination of the characteristic Debye temperature, θ_D, calculated to be 27.7 K. Interestingly, the zero-field data exhibit no lambda-like anomaly, indicating the absence of any phase transitions. Instead, the data are marked by a broad Schottky-like anomaly centered around 0.6 K. This anomaly not only shifts to higher temperatures but also increases in magnitude with the application of a magnetic field. Below the temperature range of 60-70 mK, the zero-field c_p appears to plateau.

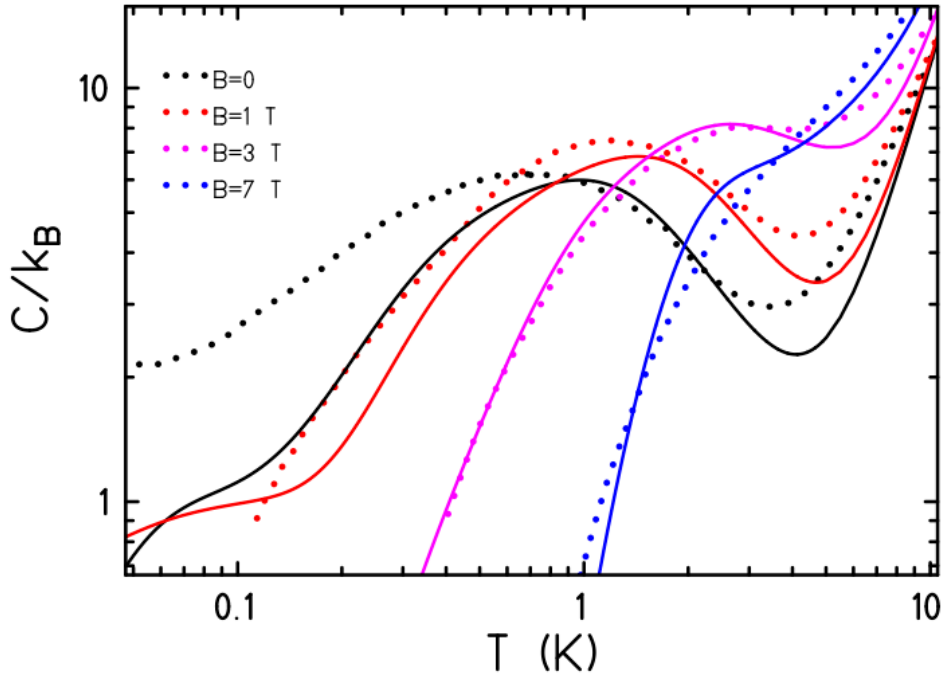

Figure 3. Heat capacity (c_p) per molecule as a function of temperature T for various magnetic fields B. The dots denote experimental values, whilst the curves are theoretical calculations.

The entropy at constant magnetic field, $S = \int c_p/T \, dT$ (**Figure S4**), was used to obtain the MCE main figure of merit, namely the magnetic entropy change ($-\Delta S_m$, **Figure S5**). The $-\Delta S_m$ reaches a maximal 23.1 J kg^{-1} K^{-1} at temperature T = 2.1 K and magnetic field change ΔB = 7 T, which corresponds to 79% of the available entropy, i.e., $R\ln(2s+1)$ = 29.1 J kg^{-1} K^{-1}. Besides indirect estimations, the MCE was also measured directly (**Figure 4**, bottom panel, and E.S.I. for details). We conducted demagnetization processes starting from a relatively high magnetic field of B = 8 T, while varying the initial temperatures T_0. As a representative example, when T_0 is set to 1.0 K, we observed that the sample temperature initially decreases linearly as the magnetic field B decreases, which aligns with the expected behavior of a paramagnet. Notably, between the magnetic field values of B = 4.8 T and 1.5 T, a bump anomaly is encountered in the temperature readings. Specifically, the temperature first experiences an increase as B decreases to 3.4 T, demonstrating an inverse MCE. Following this, the temperature steadily declines with further decreases in B down to

1.5 T. Below B = 1.5 T, there is a smaller, yet discernible bump anomaly centered at B = 0.6 T. Ultimately, upon completing the demagnetization process, the sample temperature stabilizes at T = 0.35 K. The inverse MCE observation is characteristic of frustrated topologies[6,7]. Note that the recorded temperatures are not adiabatic temperatures; hence, they do not fully reflect the potential of the system under ideal conditions. These readings are influenced not only by the magnetothermal properties of **{Gd$_9$}** but also by the unique characteristics of the sample and experimental setup used. Due to the inevitable heat exchanged between the sample and the thermal bath, lower temperatures should be achieved under adiabatic conditions.

To comprehend the overall magnetic behavior of **{Gd$_9$}**, the magnetic and magnetothermal data were modelled with the Hamiltonian of the form (1):

$$\hat{H} = -2J_1 \sum_{i<j(squares)} \hat{\vec{s}}_i \cdot \hat{\vec{s}}_j - 2J_2 \sum_{i=1}^{8} \hat{\vec{s}}_i \cdot \hat{\vec{s}}_9 + g\mu_B B \sum_{i=1}^{9} \hat{s}_i^z \qquad (1)$$

where the first term denotes the Heisenberg exchange between neighboring spins in the two squares, the second term the exchange of all spins in squares with the central spin, and the third (Zeeman) term the interaction with the external field (See **Figure 1E**). In our simulations, the single-ion anisotropy is neglected, whilst a common g-factor of 1.96 is assumed. Since the total Hilbert space has a dimension of 134,217,728, exact diagonalization of the Hamiltonian matrix is prohibitable impossible (even when using symmetry arguments); therefore, the finite-temperature Lanczos method (FTLM) is suited as an accurate approximation[25]. For the calculation, R = 100 random vectors were used to average observables[26]. **Figure 2** displays the M as $\chi_M T(T)$ at a small field (top) and $M(B)$ for various temperatures (bottom). The experimental data were used to determine the best values of J_1, J_2, and g describing both profiles. The best simulations yield J_1 = -0.09 K, J_2 = -0.10 K, and g = 1.96 (See **Figure 2** and **S6**). We estimate that the uncertainty is not bigger than 10% of these values. With this set of parameters, we calculate the magnetic contribution to c_p, as well as the isentropes of the direct MCE measurements. The experimental c_p and simulations, together with the lattice contribution, are represented in **Figure 3** as solid lines, while the simulated isentropes for ideal adiabatic conditions are depicted in **Figure 4**, together with the experimental data, and in **Figure S7** for several entropy values. The simulations, although they do not perfectly replicate the experimental data at the lowest temperatures, offer a remarkably close description.

By understanding the energy manifold of the **{Gd$_9$}** system, we can interpret the structure of its magnetic and magnetothermal data. **Figure 4** illustrates the system's unusual magnetocaloric behavior by showing how the low-lying density of states varies with the applied external magnetic field. In this context, the Zeeman energy is represented as the excitation energy above the respective ground state for each magnetic field strength. At zero field (B = 0), there is a region with a high density of states. This is followed by a range between approximately 1.5 T and 4.0 T, where the density of states is significantly lower, corresponding to a broad magnetization plateau. Beyond 4.0 T, another region of high density of states appears, which then transitions into a final region of very low density, starting at the saturation field around 4.8 T. Since entropy is related to the number of thermally accessible energy levels, regions with low density of states require higher temperatures to achieve the same level of thermal occupation as regions with higher density. This variation in thermal accessibility explains the undulating shape of the isentropes shown in the lower part of **Figure 4**.

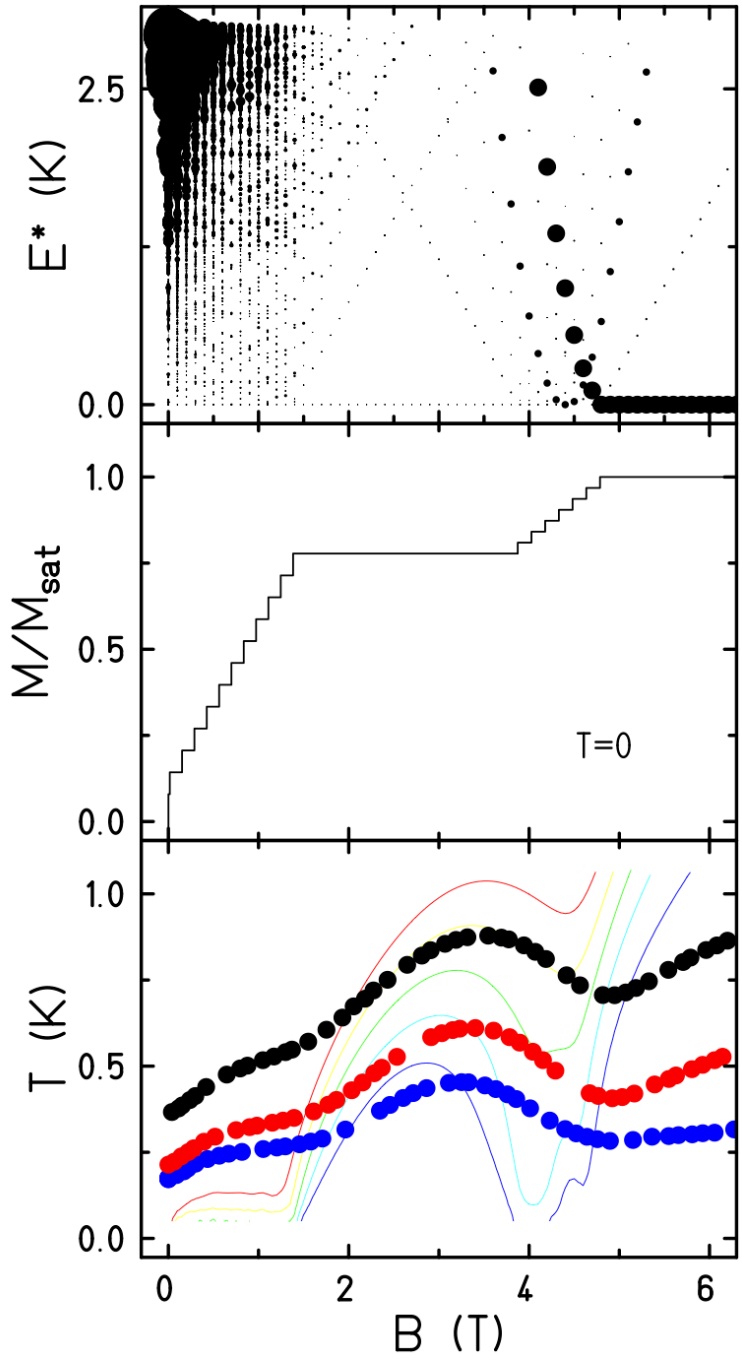

Figure 4. Top panel: Zeeman diagram of low-lying energy levels; the size of the bullet points reflects the weight of the respective energy in the FTLM. $E^* = E_i - E_0$, where E_i and E_0 are the energies of the ith and ground Zeeman states, respectively, at the respective field. Middle panel: Normalized magnetization $M(B)$ curve at zero temperature. Bottom panel: Calculated (thin curves) and directly measured (symbols) isentropes, i.e., curves of constant entropy.

CONCLUSION

This study presents a comprehensive investigation of the **{Gd$_9$}** molecular cage, revealing its potential as a model system for exploring spin frustration and magnetocaloric effects in lanthanide-based nanomagnets. The unique double-pyramidal geometry, featuring two distinct Gd^{3+} environments and a highly symmetric arrangement, leads to antiferromagnetic interactions and geometric frustration. These features manifest in the magnetic susceptibility, magnetization, and heat capacity data, with the latter showing broad Schottky anomalies and no signs of long-range magnetic

ordering. The magnetocaloric properties are particularly noteworthy: both indirect and direct measurements reveal significant entropy and temperature changes, including inverse MCE behavior—a hallmark of frustrated spin networks. Theoretical modelling using the finite-temperature Lanczos method successfully captures the essential features of the experimental data, validating the proposed exchange interactions and highlighting the role of low-lying energy states in modulating the MCE. The field-dependent density of states, with alternating regions of high and low state density, explains the observed isentropic behavior and underscores the importance of energy landscape engineering in molecular coolants. Overall, the **{Gd_9}** system exemplifies how molecular design can be leveraged to achieve tunable quantum thermodynamic responses, making it a promising platform for future studies in quantum magnetism and sub-kelvin refrigeration technologies.

ASSOCIATED CONTENT

Supporting Information

Synthetic details, experimental methods, tables and supporting figures are provided in the electronic supplementary information file. This material is available free of charge via the Internet at http://pubs.acs.org.

ACKNOLEDGMENTS

This work has received support from the EU (MSCA-DN MolCal,101119865), MICIU/AEI/10.13039/501100011033/ and ERDF/EU (PID2021-124734OB-C21, CEX2023-001286-S), Gobierno de Aragón (E11-23R, E12-23R). We acknowledge the DFG-CCR 1573 "*4f for future*" (project B4) and the Karlsruhe Nano Micro Facility (KNMF, www.kit.edu/knmf) for the provision of access to instruments at their laboratories. E.M.-P. thanks the Alexander von Humboldt Fellowship for experienced researchers for support. W.W. thanks the German Research Foundation (DFG) for the Gottfried Wilhelm Leibniz-Award, ZVN-2020_WE 4458-5. S.P.K.P thanks the European Unions's Framework Program for Research and Innovation, Horizon 2020, under the Marie Sklodowska-Curie Grant Agreement No. 847471 (QUSTEC) for funding. We also thank late. Dr. Andreas Eichhoefer, Dr. Christopher E. Anson, Dr. Asato Mitzuno, Dr. Olaf Fuhr, and Prof. Dieter Fenske for their assistance in PXRD and SC-XRD measurements, and Dr. Papri Chakraborty for the ESI-MS measurements.

COMPETING INTERESTS

The authors declare no competing financial interests.

References

(1) Moessner, R.; Ramirez, A. P. Geometrical Frustration. *Physics Today*. February 2006, pp 24–29. https://doi.org/10.1063/1.2186278.

(2) Schnack, J. Effects of Frustration on Magnetic Molecules: A Survey from Olivier Kahn until Today. *Dalton Transactions* **2010**, *39* (20), 4677. https://doi.org/10.1039/b925358k.

(3) Harrison, A. First Catch Your Hare: The Design and Synthesis of Frustrated Magnets. *Journal of Physics Condensed Matter* **2004**, *16* (11 SPEC. ISS.). https://doi.org/10.1088/0953-8984/16/11/001.

(4) Chen, H.; Manvell, A. S.; Kubus, M.; Dunstan, M. A.; Lorusso, G.; Gracia, D.; Jørgensen, M. S. B.; Kegnæs, S.; Wilhelm, F.; Rogalev, A.; Evangelisti, M.; Pedersen, K. S. Towards Frustration in Eu(Ii) Archimedean Tessellations. *Chemical Communications* **2022**, *59* (12), 1609–1612. https://doi.org/10.1039/d2cc06224k.

(5) Lorusso, G.; Sharples, J. W.; Palacios, E.; Roubeau, O.; Brechin, E. K.; Sessoli, R.; Rossin, A.; Tuna, F.; McInnes, E. J. L.; Collison, D.; Evangelisti, M. A Dense Metal-Organic Framework for Enhanced Magnetic Refrigeration. *Advanced Materials* **2013**, *25* (33), 4653–4656. https://doi.org/10.1002/adma.201301997.
(6) Sharples, J. W.; Collison, D.; McInnes, E. J. L.; Schnack, J.; Palacios, E.; Evangelisti, M. Quantum Signatures of a Molecular Nanomagnet in Direct Magnetocaloric Measurements. *Nat Commun* **2014**, *5*, 3–8. https://doi.org/10.1038/ncomms6321.
(7) Pineda, E. M.; Lorusso, G.; Zangana, K. H.; Palacios, E.; Schnack, J.; Evangelisti, M.; Winpenny, R. E. P.; McInnes, E. J. L. Observation of the Influence of Dipolar and Spin Frustration Effects on the Magnetocaloric Properties of a Trigonal Prismatic {Gd7} Molecular Nanomagnet. *Chem Sci* **2016**, *7* (8), 4891–4895. https://doi.org/10.1039/c6sc01415a.
(8) Moreno Pineda, E.; Heesing, C.; Tuna, F.; Zheng, Y. Z.; McInnes, E. J. L.; Schnack, J.; Winpenny, R. E. P. Copper Lanthanide Phosphonate Cages: Highly Symmetric {Cu3Ln9P6} and {Cu6Ln6P6} Clusters with C 3v and D3h Symmetry. *Inorg Chem* **2015**, *54* (13), 6331–6337. https://doi.org/10.1021/acs.inorgchem.5b00649.
(9) Palacios, M. A.; Moreno Pineda, E.; Sanz, S.; Inglis, R.; Pitak, M. B.; Coles, S. J.; Evangelisti, M.; Nojiri, H.; Heesing, C.; Brechin, E. K.; Schnack, J.; Winpenny, R. E. P. Copper Keplerates: High-Symmetry Magnetic Molecules. *ChemPhysChem* **2016**, *17* (1), 55–60. https://doi.org/10.1002/cphc.201500956.
(10) Schmidt, R.; Richter, J.; Schnack, J. Frustration Effects in Magnetic Molecules. *J Magn Magn Mater* **2005**, *295* (2), 164–167. https://doi.org/10.1016/j.jmmm.2005.01.009.
(11) Sessoli, R. Chilling with Magnetic Molecules. *Angewandte Chemie - International Edition* **2012**, *51* (1), 43–45. https://doi.org/10.1002/anie.201104448.
(12) Evangelisti, M.; Brechin, E. K. Recipes for Enhanced Molecular Cooling. *Dalton Transactions* **2010**, *39* (20), 4672. https://doi.org/10.1039/b926030g.
(13) Zheng, Y. Z.; Zhou, G. J.; Zheng, Z.; Winpenny, R. E. P. Molecule-Based Magnetic Coolers. *Chem Soc Rev* **2014**, *43* (5), 1462–1475. https://doi.org/10.1039/c3cs60337g.
(14) Zheng, Y. Z.; Evangelisti, M.; Winpenny, R. E. P. Co-Gd Phosphonate Complexes as Magnetic Refrigerants. *Chem Sci* **2011**, *2* (1), 99–102. https://doi.org/10.1039/c0sc00371a.
(15) Zheng, Y. Z.; Evangelisti, M.; Winpenny, R. E. P. Large Magnetocaloric Effect in a Wells-Dawson Type {Ni6Gd 6P6} Cage. *Angewandte Chemie - International Edition* **2011**, *50* (16), 3692–3695. https://doi.org/10.1002/anie.201008074.
(16) Pineda, E. M.; Tuna, F.; Zheng, Y. Z.; Teat, S. J.; Winpenny, R. E. P.; Schnack, J.; McInnes, E. J. L. Iron Lanthanide Phosphonate Clusters: {Fe6Ln6P 6} Wells-Dawson-like Structures with D3d Symmetry. *Inorg Chem* **2014**, *53* (6), 3032–3038. https://doi.org/10.1021/ic402839q.
(17) Tziotzi, T. G.; Gracia, D.; Dalgarno, S. J.; Schnack, J.; Evangelisti, M.; Brechin, E. K.; Milios, C. J. A {Gd_{12} Na_6} Molecular Quadruple-Wheel with a Record Magnetocaloric Effect at Low Magnetic Fields and Temperatures. *J Am Chem Soc* **2023**, *145* (14), 7743–7747. https://doi.org/10.1021/jacs.3c01610.
(18) Lorusso, G.; Roubeau, O.; Evangelisti, M. Rotating Magnetocaloric Effect in an Anisotropic Molecular Dimer. *Angewandte Chemie - International Edition* **2016**, *55* (10), 3360–3363. https://doi.org/10.1002/anie.201510468.
(19) Konieczny, P.; Czernia, D.; Kajiwara, T. Rotating Magnetocaloric Effect in Highly Anisotropic TbIII and DyIII Single Molecular Magnets. *Sci Rep* **2022**, *12* (1). https://doi.org/10.1038/s41598-022-20893-2.
(20) Zhitomirsky, M. E.; Honecker, A. Magnetocaloric Effect in One-Dimensional Antiferromagnets. *Journal of Statistical Mechanics: Theory and Experiment* **2004**, No. 7. https://doi.org/10.1088/1742-5468/2004/07/P07012.

(21) Honecker, A.; Wessel, S. Magnetocaloric Effect in Two-Dimensional Spin-1/2 Antiferromagnets. *Physica B Condens Matter* **2006**, *378–380* (SPEC. ISS.), 1098–1099. https://doi.org/10.1016/j.physb.2006.01.436.
(22) Derzhko, O.; Richter, J. Finite Low-Temperature Entropy of Some Strongly Frustrated Quantum Spin Lattices in the Vicinity of the Saturation Field. *Phys Rev B Condens Matter Mater Phys* **2004**, *70* (10). https://doi.org/10.1103/PhysRevB.70.104415.
(23) Alvarez, S.; Alemany, P.; Casanova, D.; Cirera, J.; Llunell, M.; Avnir, D. Shape Maps and Polyhedral Interconversion Paths in Transition Metal Chemistry. In *Coordination Chemistry Reviews*; 2005; Vol. 249, pp 1693–1708. https://doi.org/10.1016/j.ccr.2005.03.031.
(24) Gagné, O. C.; Hawthorne, F. C. Comprehensive Derivation of Bond-Valence Parameters for Ion Pairs Involving Oxygen. *Acta Crystallogr B Struct Sci Cryst Eng Mater* **2015**, *71*, 562–578. https://doi.org/10.1107/S2052520615016297.
(25) Jaklič, J.; Prelovšek, P. Lanczos Method for the Calculation of Finite-Temperature Quantities in Correlated Systems. *Phys Rev B* **1994**, *49* (7), 5065–5068. https://doi.org/10.1103/PhysRevB.49.5065.
(26) Schnack, J.; Richter, J.; Steinigeweg, R. Accuracy of the Finite-Temperature Lanczos Method Compared to Simple Typicality-Based Estimates. *Phys Rev Res* **2020**, *2* (1), 013186. https://doi.org/10.1103/PhysRevResearch.2.013186.